Photodissociation spectroscopy and dynamics of the HCCO free radical

David L. Osborn, David H. Mordaunt, Hyeon Choi, Ryan T. Bise, and Daniel M. Neumark
Department of Chemistry, University of California, Berkeley, California, 94720 and Chemical Sciences Division, Lawrence Berkeley Laboratory, Berkeley, California 94720

Celeste McMichael Rohlfing
Combustion Research Facility, Sandia National Laboratories, Livermore, California 94551-0969

(Received 25 November 1996; accepted 17 March 1997)

The photodissociation spectroscopy and dynamics of the HCCO radical have been investigated using fast radical beam photofragment translational spectroscopy. An electronic band with origin at 33 424 cm^{-1} has been identified. This band exhibits rotational resolution near the band origin, but the well-defined rovibronic structure is homogeneously broadened at higher photon energies. Based on the rotational structure this band is assigned to the $\tilde{B}\ ^2\Pi \leftarrow \tilde{X}\ ^2A''$ transition. Photofragment translational energy and angular distributions were obtained at several excitation energies. At excitation energies close to the origin, the excited, spin-forbidden $\text{CH}(a\ ^4\Sigma^-)+\text{CO}$ channel dominates, while the ground state $\text{CH}(X\ ^2\Pi)+\text{CO}$ channel is the major channel at higher photon energies. The translational energy distributions provide evidence of competition between intersystem crossing and internal conversion dissociation mechanisms, with some evidence for nonstatistical dynamics in the $\text{CH}(X\ ^2\Pi)+\text{CO}$ channel. This work yields an improved heat of formation for HCCO, $\Delta H^0_{f,298}=1.83\pm0.03$ eV. *© 1997 American Institute of Physics.* [S0021-9606(97)00324-3]

I. INTRODUCTION

The ketenyl radical (HCCO) has long been recognized as an important hydrocarbon combustion intermediate.[1] Ketenyl is the major product in the oxidation of acetylene by oxygen atoms:[2–4]

$$\text{HCCH}+\text{O}\rightarrow\text{HCCO}+\text{H} \quad 80\pm15\%, \tag{1}$$

$$\rightarrow\text{CH}_2(\tilde{X}\ ^3B_1)+\text{CO}. \tag{2}$$

Reaction (1) is a critical step in combustion chemistry because acetylene is a common intermediate in combustion of both aliphatic[5] and aromatic[6] hydrocarbons, and is removed primarily by reaction with oxygen atoms.[7] It is therefore of considerable interest to characterize the spectroscopy and thermochemistry of HCCO, so that its concentration can be monitored in combustion environments, and its reactions can be predicted with greater confidence in combustion kinetics models. Recently, we reported the first unambiguous observation of an ultraviolet spectrum of the ketenyl radical in a fast radical beam photodissociation experiment;[8] prior to this work, spectroscopic information on HCCO had been limited to the microwave region,[9,10] a single vibrational band in the infrared,[11] and tentative reports of an electronic transition.[12,13] In this article we present a full discussion of the electronic spectroscopy and photodissociation dynamics of the HCCO radical and compare this system with the closely related CH_2CHO[14] and CH_3O[15] intermediates.

The importance of the HCCO radical in combustion has motivated several kinetics[1–4,16–25] and spectroscopy experiments,[8–13,26–28] as well as theoretical investigations[29–39] over the years. Fenimore and Jones[40] first proposed that HCCO is formed in the reaction of oxygen atoms with C_2H_2, a prediction verified by Jones and Bayes using photoionization mass spectrometry.[16] A crossed molecular beam study of the $\text{C}_2\text{H}_2+\text{O}$ reaction by Schmoltner *et al.*[21] showed unambiguously that combustion of C_2H_2 proceeds via reactions (1) and (2) under collisionless conditions. The many kinetic studies involving both the production of HCCO from $\text{C}_2\text{H}_2+\text{O}$, and the destruction of HCCO through various reactions have been summarized by Peeters *et al.*[4,18] Of particular interest to our work, Herbert *et al.*[25] have conducted kinetics measurements from 23 to 584 K on vibrational relaxation of CH $[X(^2\Pi);\ v=1]$ by CO; the fast rates observed are indicative of formation of an HCCO complex.

The ground electronic state of the HCCO radical has been characterized by several spectroscopic methods. Oakes *et al.* obtained the electron affinity of HCCO and determined the heat of formation of the radical by photoelectron spectroscopy of HCCO^-.[26] The microwave spectra of HCCO and DCCO due to Endo *et al.*[9] showed that HCCO is bent, although it is effectively described as quasilinear. From this work the ground electronic state was determined to be of $^2A''$ symmetry. The large a-axis spin-rotation constant and its anomalous dependence on K_a were attributed to perturbation of the ground state by a low-lying $^2A'$ state. In the infrared region, Jacox and Olsen[28] assigned a matrix absorption at 2020 cm^{-1} to HCCO. This band was later identified at 2023 cm^{-1} in the gas phase and the rotational structure analyzed in detail by Unfried *et al.*[11]

The characterization of the excited electronic states of HCCO has been more problematic. Two electronic absorption bands of HCCO were reported by Krishnamachari and Venkatasubramanian,[12] with band origins at 27 262 and 29 989 cm^{-1}. The carrier of these bands was produced by flash photolysis of oxazole and isoxazole, and their assignment to the HCCO radical has been questioned.[37] A laser

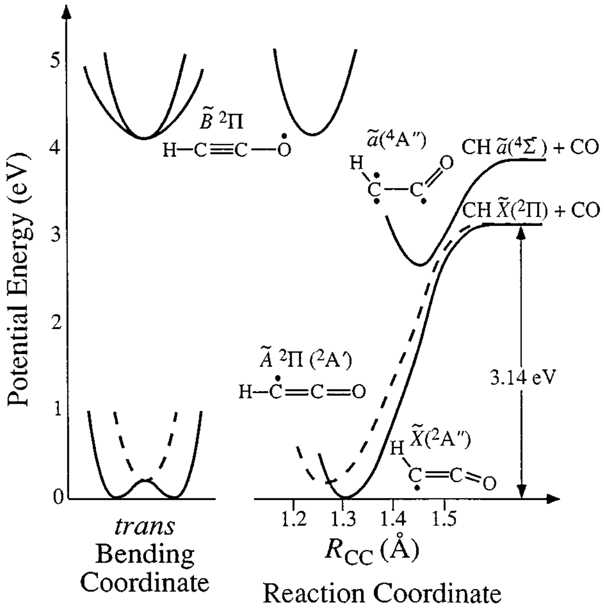

FIG. 1. Schematic of potential energy surfaces for the HCCO radical.

induced fluorescence (LIF) spectrum of HCCO, produced by reaction of O atoms with C_2H_2, was also reported,[13] although the fluorescence was later shown to have arisen entirely from CH_2O.[27]

The experimental results on the ground state of HCCO radical are consistent with *ab initio* electronic structure calculations by Goddard,[31] Kim and Shavitt,[33] and Szalay *et al.*,[34,37,38] providing considerable insight into the excited state structure. According to these calculations, the bent ground state, $\tilde{X}(^2A'')$, and the linear $\tilde{A}(^2A')[^2\Pi]$ state are a Renner–Teller (RT) pair derived from a linear $^2\Pi$ configuration. The *ab initio* splitting between these two states is 981 cm^{-1},[33] in reasonable agreement with that estimated from the microwave analysis. Kim and Shavitt[33] predicted a higher-lying RT pair $2(^2\Pi)$, comprised of the bent $\tilde{B}(^2A')$ state at 33 000 cm^{-1} and the linear $\tilde{C}(^2A'')[^2\Pi]$ state at 33 300 cm^{-1} above the ground state. Szalay *et al.*[37,38] have recently studied the same $2(^2\Pi)$ electronic states and found both RT components to be linear, lying 36 000 cm^{-1} above the ground state. Nguyen *et al.*[36] predicted a higher-lying linear $^2\Sigma^+$ state at ca. 53 000 cm^{-1}. Hu *et al.*[35] have characterized the lowest quartet state of HCCO, a *cis*-bent $\tilde{a}(^4A'')$ state, which is predicted to lie 19 000 cm^{-1} above the $\tilde{X}(^2A'')$ state. A recent article by Yarkony explores the intersection of the $\tilde{a}$ state with the two low-lying doublet states.[39] Figure 1 shows a qualitative picture of the relevant potential energy surfaces of HCCO based on the calculations in Refs. 35 and 37.

In our experiment, a *mass-selected* source of neutral HCCO radicals is prepared by laser photodetachment of the $HCCO^-$ ion. A second laser then probes the dissociative electronically excited states of these radicals, ensuring that all our data arises solely from the ketenyl radical. Our experiment directly assesses whether photodissociation occurs; it also identifies and characterizes the nascent photofragments.

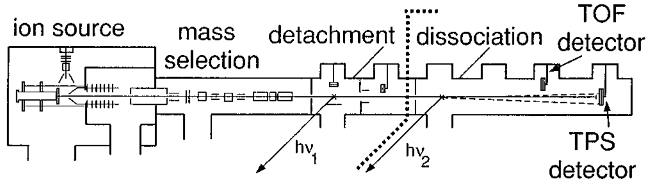

FIG. 2. Fast radical beam translational spectrometer. The dotted line separates the radical production section on the left from the actual photodissociation experiment on the right.

For the ketenyl radical, three dissociation channels are energetically allowed for photon energies in this study:

$$\text{HCCO } \tilde{X}(^2A'')$$

$$\xrightarrow{h\nu}\text{CH } X(^2\Pi)+\text{CO } X(^1\Sigma^+)$$

$$\Delta H_0=3.14\pm0.03 \text{ eV (Ref. 8)}, \qquad \text{(I)}$$

$$\rightarrow\text{CH } a(^4\Sigma^-)+\text{CO } X(^1\Sigma^+)$$

$$\Delta H_0=3.88\pm0.03 \text{ eV (Ref. 8)}, \qquad \text{(II)}$$

$$\rightarrow\text{H}(^2S)+\text{CCO } \tilde{X}(^3\Sigma^-)$$

$$\Delta H_0=4.36\pm0.05 \text{ eV (Refs. 8, 41, 42)}. \qquad \text{(III)}$$

Channels I and II are observed in our experiment. We observe structure in the photofragment yield spectrum of HCCO, and present a rotational analysis of the $\tilde{B}(^2\Pi)\leftarrow\tilde{X}(^2A'')$ transition. From translational energy and angular distributions of the fragments, we obtain information on the rotational and vibrational product state distributions of the fragments. The experimental results and data analysis are presented in Secs. III and IV. Based on our experimental data, we develop a dissociation mechanism in Sec. V, and discuss the dependence of intersystem crossing and internal conversion on photon energy.

II. EXPERIMENT

The experimental apparatus shown in Fig. 2 has been described in detail elsewhere,[43,44] and only a brief description of the technique is given here. In the first section of the apparatus, a pulsed free jet expansion of the gas mixture C_2H_2:N_2O:O_2:Ne (mole fraction 1:3:6:90) is formed in the source region. $HCCO^-$ is generated by a pulsed electric discharge[45] in the throat of this expansion. The core of the free jet passes through a 3-mm diameter skimmer and the anions are accelerated to 8 keV. Mass-separation of the ions is accomplished using a collinear Bakker-type[46] time-of-flight mass spectrometer. After collimation of the ion beam by a 1-mm pinhole, the output of a pulsed dye laser is timed such that it photodetaches only those anions with $m/e=41$, producing a packet of mass-selected neutral free radicals. Any remaining ions are deflected from the beam. The photodetachment energy ($h\nu = 19\,230$ cm^{-1}) is just above threshold,[26] producing radicals in vibrational ground state.

In the second section of the apparatus, the radicals are collimated by a final 1-mm pinhole and intersect a second pulsed dye laser operating in the ultraviolet. If photodissociation occurs, fragments recoiling out of the parent radical beam are detected with high sensitivity, *without* an ionization step, using microchannel plate detectors. Photodissociation occurs under collisionless conditions (10^{-9} Torr), and two types of experiments are performed. First, the photofragment yield (PFY) spectrum is obtained by integrating the total fragment signal as a function of photodissociation laser wavelength. Second, at various fixed photon energies, the dissociation dynamics are investigated by detecting both fragments in coincidence from a single parent radical dissociation event. We measure the photofragment translational energy and angular distributions using a time- and position-sensitive (TPS) wedge and strip anode detector.[47,48] The identity of the photofragments is determined by measuring the individual recoils of each fragment from the radical beam axis to give the fragment mass ratio, m_1/m_2, by conservation of linear momentum. Angular distributions of the photofragments are defined with respect to the **E** vector of the linearly polarized dissociation laser. In the present experiments the translational energy resolution is given by $\Delta E_T/E_T = 2.2\%$.

The doubled output of the photodissociation laser has a bandwidth of ≈ 0.3 cm^{-1} when operated with a grating as its only tuning element. In this mode the PFY spectra are calibrated at many different frequencies throughout the scanned range against the absorption spectrum of I_2,[49] with an absolute accuracy of 1 cm^{-1} or better. The bandwidth of the laser is reduced to ≈ 0.08 cm^{-1} with the incorporation of an intracavity etalon. PFY spectra acquired in this configuration are calibrated against simultaneously collected I_2 absorption spectra yielding an absolute accuracy of 0.05 cm^{-1}.

As discussed previously,[14] the coincidence detection scheme is useful only when $m_1/m_2 \leqslant \sim 5$. In order to probe for channel III products, we utilize a noncoincidence time-of-flight detection scheme when dissociating the isotope DCCO of the ketenyl radical. Unlike the coincidence detection method described above, this experiment would be sensitive to the product channel D+CCO, and has been used to identify a D atom loss channel in the photodissociation of the vinoxy radical.[14] No evidence for channel III is observed. For experimental reasons it is difficult to place an upper bound on the importance of this channel, but it is almost certainly not a major pathway in the ultraviolet dissociation of HCCO.

III. RESULTS

A. Photofragment yield spectra

The PFY spectrum of HCCO from 33 000 to 48 000 cm^{-1}, shown in Fig. 3, indicates the energies at which HCCO absorbs a photon and dissociates. In the limit that the quantum yield for dissociation $\Phi_{\text{Diss}} = 1$, the PFY spectrum is identical to the absorption spectrum. This spectrum shows unambiguously that dissociation occurs after UV excitation of HCCO. The lowest energy at which we observe dissociation is $h\nu \approx 33\,400$ cm^{-1}, which is tentatively assigned below as the origin of this electronic band.

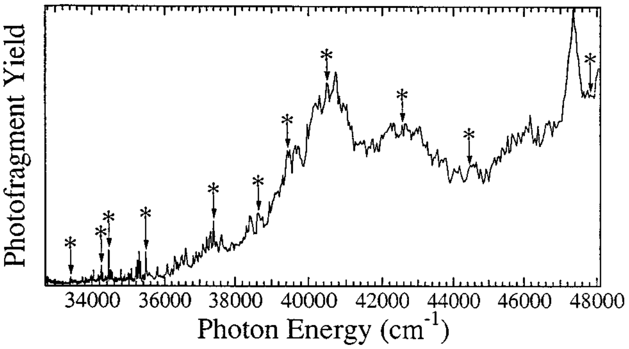

FIG. 3. Overall photofragment yield (PFY) spectrum of HCCO. Photodissociation dynamics data are acquired at the peaks marked with (*). The lowest energy asterisk marks the origin transition.

The PFY spectrum shows clear vibrational structure towards the red, as seen more clearly in Fig. 4, which displays the first 4000 cm^{-1} of the spectrum. In addition, rotational structure is resolved at the origin and in a few vibrational bands; two such spectra are shown in Fig. 5. The spectrum in Fig. 3 shows that the photofragment yield increases significantly with increasing photon energy, concurrent with broadening of the vibrational structure. Above 41 000 cm^{-1}, no sharp vibrational transitions are apparent, although broad undulations in the spectrum continue to the highest energies studied.

The spectroscopic information we obtain from HCCO is derived from the structured region in the first 4000 cm^{-1} of the PFY spectrum, shown in Fig. 4. The structure represents extended vibrational progressions in the excited electronic state. In this spectrum, the first 1900 cm^{-1} were acquired with a laser step size of 0.3 cm^{-1}, equal to the laser band-

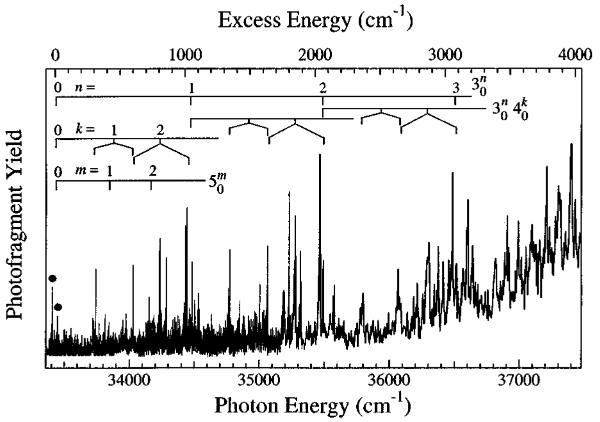

FIG. 4. Vibrational structure in the first 4000 cm^{-1} of the PFY spectrum. Excess energy is given relative to the rovibronic origin at 33 423.92 cm^{-1}. The vibrational progression in the ν_3 CCO symmetric stretch and the two bending modes ν_4 and ν_5 are indicated by the combs, with the Renner–Teller splitting shown for ν_4. The F_1 and F_2 branches of the 0_0^0 transition are indicated with (●).

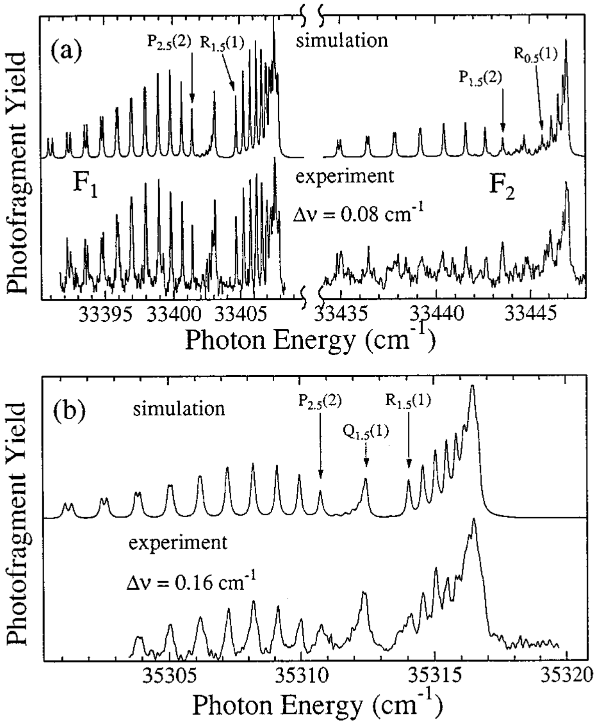

FIG. 5. Rotationally resolved PFY spectra of HCCO. (a) The origin transition shows splitting into both F_1 and F_2 branches, with asymmetry doubling resolved in the F_1 branch. The experimental linewidth is instrument limited at 0.08 cm^{-1}. (b) The F_1 branch of an unassigned vibrational transition $\approx$1 900 cm^{-1} above the origin. The experimental linewidth is broadened to 0.16 cm^{-1}.

width. Beyond this region the step size is increased to 3 cm^{-1}. The coarser step size expedites data acquisition with little loss of vibrational structure information.

A few of the transitions in Fig. 4 were examined at higher resolution (0.08 cm^{-1} laser bandwidth); two rotationally resolved spectra are shown in Fig. 5. The two bands in Fig. 5(a) are taken near the onset of dissociation and correspond to the two peaks indicated by a (●) in Fig. 4. In the lower frequency band centered at 33 403 cm^{-1}, one can easily recognize P, Q, and R branches with a prominent band head occurring in the R branch. The experimental linewidths are instrumentally narrow (i.e., 0.08 cm^{-1}) in Fig. 5(a).

While many of the vibrational bands do not reveal rotational structure at our resolution, a few vibrationally excited bands were rotationally resolved, one of which is shown in Fig. 5(b), ca. 1900 cm^{-1} above the origin transition. Again a simple P,Q,R, structure is apparent, although the peaks are now noticeably broader.

B. Translational energy and angular distributions

Once the dependence of photodissociation on photon energy has been mapped out for the ketenyl radical, its photodissociation dynamics can be explored at selected photon energies using the TPS detector. First, the identity of the photoproducts is ascertained by conservation of linear momentum. At all photon energies, the only fragments observed are CH+CO, as expected for the coincidence detector configuration. With knowledge of the fragment masses, we obtain the coupled translational energy and angular distribution, $P(E_T,\theta)$, by direct inversion of the data.[43] The two dimensional $P(E_T,\theta)$ distribution can then be separated into an angle-independent translational energy distribution $P(E_T)$, and an energy-dependent anisotropy parameter $\beta(E_T)$,[50] that describes the angular distribution of the fragments:

$$P(E_T,\theta)=P(E_T)\cdot\{1+\beta(E_T)\cdot P_2(\cos\,\theta)\}, \tag{3}$$

where $P_2(\cos\,\theta)$ is the second Legendre polynomial. The limiting cases of $\sin^2\theta$ and $\cos^2\theta$ angular distributions are given by $\beta=-1$ and $+2$, respectively. Together, the $P(E_T)$ and $\beta(E_T)$ distributions can yield detailed information on the dynamics of the dissociation process. The procedure for extracting the $P(E_T)$ and $\beta(E_T)$ distributions from the data have been described in detail elsewhere.[43] Photodissociation dynamics experiments were performed at each photon energy marked with (*) in Fig. 3. The resulting $P(E_T)$ and $\beta(E_T)$ distributions are shown in Fig. 6.

The $P(E_T)$ distributions show several trends with increasing photon energy. Two features are visible at the lowest excitation energies in Figs. 6(a)–(c): a dominant peak centered at $E_T=0.20-0.25$ eV, and a weak, broad feature centered at $E_T=0.75$ eV that gains intensity with photon energy. As discussed in our previous paper, and in more detail in Sec. IV C below, these features correspond to channels II and I, respectively. The vertical dashed lines in Fig. 6 show the maximum kinetic energies allowed for the two channels. In Fig. 6(d), the two features appear to have approximately the same intensity and are difficult to separate. As the photon energy increases further, the appearance of the spectra change, until they are dominated by a single peak at $E_T=0.8-0.9$ eV superimposed on a broad background. This peak position is essentially independent of excitation energy over a 10 000 cm^{-1} range. At the highest energy studied, 47 831 cm^{-1}, the width of the $P(E_T)$ distribution broadens considerably. At all photon energies, the $P(E_T)$ distributions extend to the maximum available kinetic energy for channel I.

The energy-dependent anisotropy parameter, $\beta(E_T)$, is plotted as a function of E_T in Fig. 6; we do not report $\beta(E_T)$ for $E_T<0.3$ eV due to the limited range of laboratory scattering angles which can be detected for these small recoils. In all cases $\beta(E_T)\geqslant 0$, implying a parallel electric dipole transition.[50] Several trends in $\beta(E_T)$ are apparent. At low photon energy, $\beta(E_T)$ increases with E_T, whereas at higher photon energy [Figs. 6(g)–(j)], there is a broad maximum in $\beta(E_T)$ whose center approximately coincides with the peak at 0.9 eV in the $P(E_T)$ distribution. For $h\nu\geqslant 35\,464$ cm^{-1}, the energy-averaged anisotropy $\langle\beta\rangle$ (Fig. 6) tends to be an increasing function of photon energy, with individual values of β as high as $\beta(E_T=0.9\text{ eV})=1.0$ for $h\nu=40\,488$ cm^{-1}. At still higher photon energies $\langle\beta\rangle$ decreases in magnitude again.

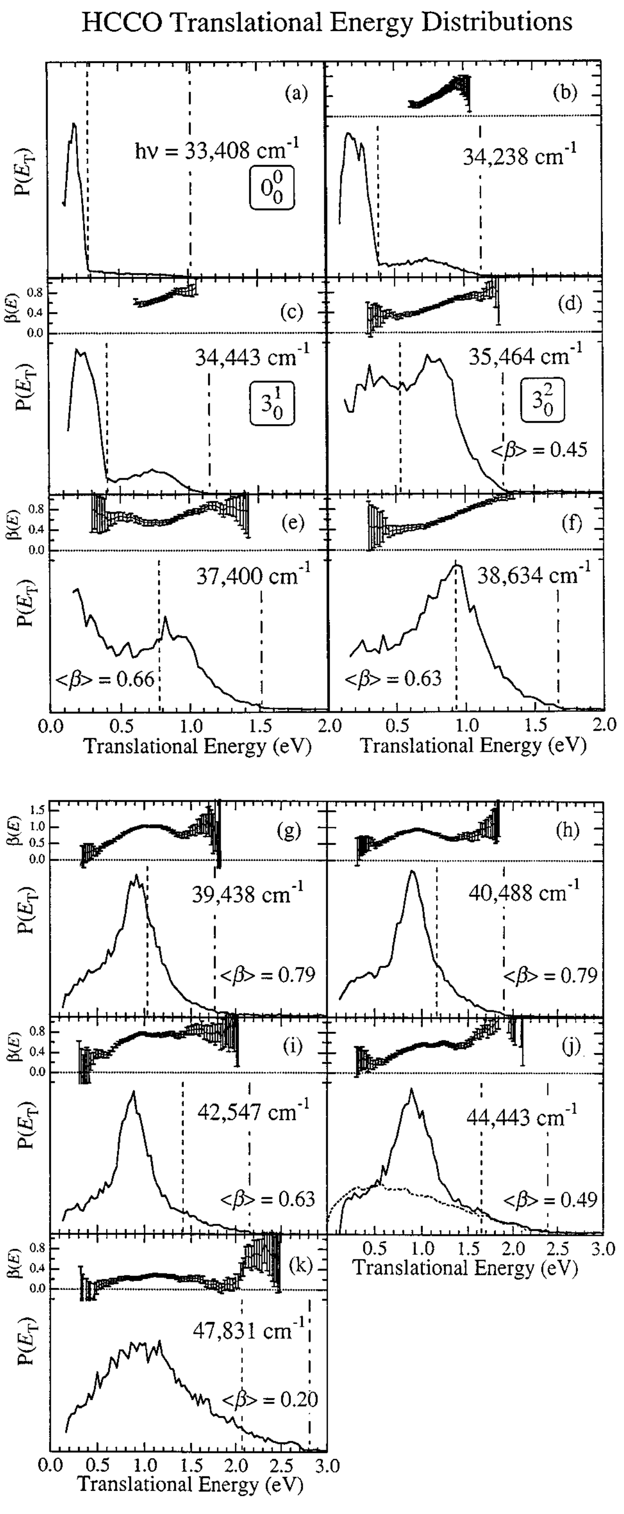

FIG. 6. Translational energy distributions, $P(E_T)$, and anisotropy parameter distributions, $\beta(E_T)$, for the marked transitions in Fig. 3. In each case the photon energy are specified. The vertical lines indicate $E_T^{\max}$ for the production of channel I (———) and II products (-----). In panel (j) a prior distribution is also plotted using a dashed line. The $\beta(E_T)$ distributions are not determined for E_T below 0.3 eV (see text). For greater clarity, $\beta(E_T)$ is only plotted between 0 and 1, not its full range of -1 to 2. Energy-averaged values $\langle\beta\rangle$ are also indicated.

C. Electronic structure calculations

One issue which has not been addressed in previous *ab initio* calculations on the HCCO radical is the nature of the $\tilde{X}(^2A'')$ state as the C–C bond is elongated and finally dissociated. We have performed *ab initio* calculations to determine whether a barrier exists on the way to product formation. For reference, the molecular orbital configurations of the relevant valence states of HCCO are given in Table I. In order to properly describe the dissociation into CH+CO, we have used the multi-configurational complete active space self-consistent field[51] (CASSCF) method from the GAUSSIAN 94 package[52] of programs. An active space of nine electrons in eight orbitals [CAS(9,8)] was chosen as the three $a''\ p_\pi$ orbitals, the three $a'\ p_\pi$ orbitals, and the C–C σ and σ^* orbitals. The 6-31G^* basis set was used for this work.

The r_{CC} bond length was increased incrementally, optimizing at each increment the remaining degrees of freedom, in order to determine the minimum energy pathway to products. Referring to Fig. 1, we find no evidence for a barrier on the $\tilde{X}(^2A'')$ surface along the minimum energy path out to the longest C–C bond length calculated, $r_{\mathrm{CC}}=2.7$ Å. If a barrier of significant magnitude existed, it would almost certainly occur for $r_{\mathrm{CC}}<2.7$ Å. The absence of an exit barrier on the ground state is supported experimentally by rate constant measurements over a wide range of temperatures for the relaxation of CH[$X(^2\Pi)$; $v=1$] by CO and N_2.[25] Because the $\tilde{X}(^2A'')$ and the $\tilde{A}(^2A')$ states are a Renner-Teller pair, they correlate to the same doubly degenerate asymptote CH $X(^2\Pi)$+CO $X(^1\Sigma^+)$, and we do not expect a barrier on the $\tilde{A}$ state surface because the RT splitting should decrease as r_{CC} increases.

IV. ANALYSIS

This section is divided into three categories dealing with the details in the analysis of the rotational and vibrational transitions observed in the PFY spectra, and the form of the photofragment $P(E_T)$ distributions.

A. Rotational structure

Analysis of the rotationally resolved PFY spectra in Fig. 5 is the first step in characterizing the electronic transition seen in HCCO. Fortunately, the $\tilde{X}(^2A'')$ ground state of ketenyl has been characterized from the microwave spectroscopy of Endo *et al.*[9] According to this work, the ground state has a linear or nearly linear CCO backbone, but ∠HCC $=138.7°$, placing the H atom well away from the a-axis. Due to the low mass of the H atom, HCCO $\tilde{X}(^2A'')$ is a near prolate symmetric top, with an asymmetry parameter near unity ($\kappa_{\mathrm{asym}}=-0.9998$). The microwave rotational spectra were analyzed using a Hund's case (b) Hamiltonian, although Unfried *et al.* point out that for $K_a\neq 0$ the coupling is closer to case (a).[11] However, it is less convenient to use a case (a) Hamiltonian since the ground state is nonlinear, and we therefore follow the precedent of Endo *et al.*,[9] utilizing a case (b) Hamiltonian to analyze the rotational structure of ketenyl.

With this background, we can examine in more detail the PFY spectrum of the lower energy band in Fig. 5(a), whose line positions are given in Table II. Based on the Hönl–London factors for a symmetric top,[53] the fact that a Q

TABLE I. Molecular orbital configurations of HCCO electronic states.

Orbital character	$\tilde{X}(^2A'')$	$\tilde{A}(^2A')[^2\Pi]$	$\tilde{a}(^4A'')$	$\tilde{B}(^2\Pi)$[a]
O$(1s)$	$(1a')^2$	$(1\sigma)^2$	$(1a')^2$	$(1\sigma)^2$
C$(1s)$	$(2a')^2$	$(2\sigma)^2$	$(2a')^2$	$(2\sigma)^2$
C$(1s)$	$(3a')^2$	$(3\sigma)^2$	$(3a')^2$	$(3\sigma)^2$
O$(2s)$	$(4a')^2$	$(4\sigma)^2$	$(4a')^2$	$(4\sigma)^2$
CH(σ)	$(5a')^2$	$(5\sigma)^2$	$(5a')^2$	$(5\sigma)^2$
CO(σ)	$(6a')^2$	$(6\sigma)^2$	$(6a')^2$	$(6\sigma)^2$
CC(σ)	$(7a')^2$	$(7\sigma)^2$	$(7a')^2$	$(7\sigma)^2$
CO(π_x)[b]	$(8a')^2$	$(1\pi_x)^2$	$(8a')^2$	$(1\pi_x)^1$ $(1\pi_x)^2$
CO(π_y)	$(1a'')^2$	$(1\pi_y)^2$	$(1a'')^2$	$(1\pi_y)^2$ $(1\pi_y)^1$
CCO(π_x)	$(9a')^2$	$(2\pi_x)^1$	$(9a')^1$	$(2\pi_x)^2$
CCO(π_y)	$(2a'')^1$	$(2\pi_y)^2$	$(2a'')^1$	$(2\pi_y)^2$
CCO(π_x^*)	$(10a')^0$	$(3\pi_x)^0$	$(10a')^1$	$(3\pi_x)^0$
CCO(π_y^*)	$(3a'')^0$	$(3\pi_y)^0$	$(3a'')^0$	$(3\pi_y)^0$

[a] At linearity the π_x and π_y orbitals of the $\tilde{B}$ state are degenerate. In the case of strong Renner–Teller coupling such that the lower RT state is nonlinear, as found in Ref. 33, the two resulting electronic states are described by the left and right configurations, respectively, of the CO(π) orbitals in this column.

[b] The π orbitals of the CCO backbone are analogous to the three π orbitals of linear C_3, which have zero, one, and two nodes in the xy plane, respectively, as a function of increasing energy.

branch is observed but does not dominate the spectrum implies a parallel, a-type rotational transition for which $\Delta K_a = 0$. Furthermore, the electronic transition cannot be $K_a' = 0 \leftarrow K_a'' = 0$ because: (i) in this case the Q branch would be vanishingly small (forbidden in the symmetric top limit); and (ii) asymmetry doubling, which we resolve in the P branch, is not allowed for $K_a = 0$ levels.

Analysis of the spectra using combination differences shows that half-integral values of J are required, i.e., Hund's case (a) coupling. The first lines in the P and R branches are identified as $P_{2.5}(2)$ and $R_{1.5}(1)$, where the notation is $\Delta J_{J''}(N'')$. All the transitions in this band have $J = N + 1/2$ in both ground and excited states, i.e., they represent $F_1 \leftarrow F_1$ components. Although it is perhaps not clear on inspection, the higher energy band (by $\approx 47\ \mathrm{cm}^{-1}$) in Fig. 5(a) corresponds to the $F_2 \leftarrow F_2$ components of this same transition. It follows, based on the identity of the first rotational transitions, that the band in Fig. 5(a) must be assigned as $K_a' = 1 \leftarrow K_a'' = 1$. The fact that we can observe any asymmetry doubling at all (given our limited laser resolution) for this near prolate asymmetric top supports this assignment, since asymmetry doubling is largest for $K_a = 1$.

At this point we need to determine the geometry and electronic configuration of the upper electronic state. As discussed by Herzberg,[53] there are several characteristics which differentiate the rotational spectrum of a bent←bent vs a linear←bent electronic transition. There are two features in Fig. 5(a) that suggest that the upper state is a linear $^2\Pi$ state: (a) the absence of a $K_a' = 0 \leftarrow K_a'' = 0$ sub-band, and (b) the 47 cm^{-1} separation between the $F_1 \leftarrow F_1$ and $F_2 \leftarrow F_2$ components. The absence of the $0 \leftarrow 0$ sub-band is expected at the vibrational origin of a transition to a linear $^2\Pi$ state, because K' must equal 1 for the $v = 0$ level of a Π state $(K' = |\Lambda + l| = 1 + 0 = 1)$. Moreover, the magnitude of the 47 cm^{-1} separation is more characteristic of the spin-orbit splitting in a linear $^2\Pi$ state than the spin-rotation splitting in a nonlinear state.

Based on this evidence, we analyze the spectra in Fig. 5 as transitions from $K_a'' = 1$ levels of a slightly asymmetric rotor to the $K' = 1$ levels of a linear $^2\Pi$ state. For the extraction of spectroscopic constants, we choose the same Hamiltonian as Unfried *et al.*:[11]

$$\mathbf{H} = \mathbf{H}_{\mathrm{rot}} + \mathbf{H}_{\mathrm{sr}}, \tag{4}$$

where $\mathbf{H}_{\mathrm{rot}}$ is a Watson S-reduced asymmetric rotor Hamiltonian,[54] and $\mathbf{H}_{\mathrm{sr}}$ accounts for the spin-rotation interaction.[55,56] Due to the lower resolution of our present work compared to microwave spectroscopy, several of the higher order terms for the ground state are not required. The molecular constants are fit to the data using a nonlinear least-squares method. In all cases we fix the values of the ground state parameters to the microwave values.[9] The least-squares fit provides our best values for the rotational constant B', the spin-rotation constants $\kappa' (\equiv \epsilon_{aa}' - \epsilon_{bb}')$ and $\mu' (\equiv \epsilon_{bb}')$, and the band origin ν_0, of the linear excited state (Tables II and III).

A simulation based on these constants is shown in the Fig. 5(a). The intensities of the simulated lines were obtained from the Hönl–London factors for a symmetric top. The best match with the data is found for a rotational temperature $T = 35$ K. Taking into account the large rotational constant $A'' = 41.46\ \mathrm{cm}^{-1}$, only those ground state levels with $K_a'' = 0$ or 1 should be significantly populated in the radical beam, since $k_b T = 24\ \mathrm{cm}^{-1}$, and only those radicals with $K_a'' = 1$ contribute. The simulated stick spectrum is convoluted with a 0.08-cm^{-1} FWHM Gaussian line shape representing the laser bandwidth with the etalon installed, and the agreement with the measured linewidths is quantitative.

By the same procedure, the band in Fig. 5(b) with $\approx 1900\ \mathrm{cm}^{-1}$ more vibrational energy can be assigned, the spectroscopic constants extracted, and the spectrum simulated, with the results given in Table III. In this case only the spectrum of the F_1 branch was obtained. The most striking

TABLE II. Rotational assignments and frequencies for 0_0^0.

$K'_{K'_aK'_c}$	$N''_{K''_aK''_c}$	Branch	Observed[a]	Obs.-calc.
1_{11}	2_{12}	F_1	33 401.39	−0.01
1_{10}	2_{11}	F_1	33 401.39	−0.00
2_{12}	3_{13}	F_1	33 400.63	0.01
2_{11}	3_{12}	F_1	33 400.63	0.02
3_{13}	4_{14}	F_1	33 399.80	0.00
3_{12}	4_{13}	F_1	33 399.80	0.03
4_{14}	5_{15}	F_1	33 398.94	0.02
4_{13}	5_{14}	F_1	33 398.94	0.06
5_{15}	6_{16}	F_1	33 398.00	−0.01
5_{14}	6_{15}	F_1	33 398.00	0.06
6_{16}	7_{17}	F_1	33 396.96	−0.07
6_{15}	7_{16}	F_1	33 396.96	0.03
7_{17}	8_{18}	F_1	33 395.99	0.01
7_{16}	8_{17}	F_1	33 395.86	−0.00
8_{18}	9_{19}	F_1	33 394.87	−0.01
8_{17}	9_{18}	F_1	33 394.71	−0.00
9_{19}	$10_{1,10}$	F_1	33 393.71	0.01
9_{18}	10_{19}	F_1	33 393.51	0.01
$10_{1,10}$	$11_{1,11}$	F_1	33 392.46	−0.00
10_{19}	$11_{1,10}$	F_1	33 392.22	0.00
1_{10}	1_{11}	F_1	33 403.08	−0.01
1_{11}	1_{10}	F_1	33 403.08	−0.01
3_{12}	3_{13}	F_1	33 402.87	−0.00
3_{13}	3_{12}	F_1	33 402.87	0.01
4_{13}	4_{14}	F_1	33 402.67	−0.03
4_{14}	4_{13}	F_1	33 402.67	0.00
5_{14}	5_{15}	F_1	33 402.45	−0.02
5_{15}	5_{14}	F_1	33 402.45	0.03
2_{12}	1_{11}	F_1	33 404.69	−0.01
2_{11}	1_{10}	F_1	33 404.69	−0.01
3_{13}	2_{12}	F_1	33 405.23	−0.02
3_{12}	2_{11}	F_1	33 405.23	−0.01
4_{14}	3_{13}	F_1	33 405.75	−0.01
4_{13}	3_{12}	F_1	33 405.75	0.00
5_{15}	4_{14}	F_1	33 406.22	−0.00
5_{14}	4_{13}	F_1	33 406.22	0.02
6_{16}	5_{15}	F_1	33 406.62	−0.02
6_{15}	5_{14}	F_1	33 406.62	−0.02
7_{17}	6_{16}	F_1	33 406.98	−0.03
7_{16}	6_{15}	F_1	33 406.98	0.04
1_{11}	2_{12}	F_2	33 443.50	−0.04
1_{10}	2_{11}	F_2	33 443.50	−0.03
2_{12}	3_{13}	F_2	33 442.63	0.02
2_{11}	3_{12}	F_2	33 442.63	0.04
3_{13}	4_{14}	F_2	33 441.56	−0.01
3_{12}	4_{13}	F_2	33 441.56	0.01
5_{15}	6_{16}	F_2	33 439.22	0.00
5_{14}	6_{15}	F_2	33 439.22	0.06
7_{17}	8_{18}	F_2	33 436.47	−0.04
7_{16}	8_{17}	F_2	33 436.47	0.08
8_{18}	9_{19}	F_2	33 435.03	0.01
8_{17}	9_{18}	F_2	33 434.81	−0.05

[a] For transitions where the asymmetry doubling is not resolved, both $K_c = N$ and $K_c = N-1$ components are assigned to the single observed line, so that these transitions have the proper statistical weight.

TABLE III. Spectroscopic constants.

	$\tilde{X}(^2A'')$[a]	$\tilde{B}(^2\Pi)0_0^0$	$\tilde{B}(^2\Pi)$1900-cm^{-1} band
A	41.46	-	-
B	0.363 477 7	0.3242±0.0002	0.3201±0.0003
C	0.359 130 6		-
κ[b]	−8.266	−46.76±0.04	-
μ[c]	−0.000 489	−0.06±0.03	-
ν_0	-	33 423.92±0.02	35 332.82±0.02[d]

[a] Ground state constants were fixed at these values from Ref. 9.

[b] $\kappa = \epsilon_{aa} - (\epsilon_{bb} + \epsilon_{cc})/2$.

[c] $\mu = (\epsilon_{bb} + \epsilon_{cc})/2$.

[d] The value of κ was assumed to be identical to the value obtained in the origin transition.

feature of this band is the increase in linewidth to $\Delta\nu = 0.16$ cm^{-1}, twice the instrumental resolution.

The increased linewidths are most plausibly the result of lifetime broadening. The two significant contributions to our line shapes are a Gaussian component from the laser bandwidth and a Lorentzian component due to predissociation induced lifetime broadening. Deconvolution gives a rough lower limit on the lifetime of bands in Fig. 5(a) (characterized by instrumentally narrow lines) of $\tau > 300$ ps. The broader lines in Fig. 5(b) correspond to an excited state lifetime of $\tau = 90$ ps.

In summary, the rotationally resolved PFY spectra of HCCO indicate that the excited electronic state is a linear $^2\Pi$ state. Our results are entirely consistent with the molecular constants derived from microwave spectroscopy for the $\tilde{X}(^2A'')$ state. A large a-axis spin-rotation constant, $\epsilon'_{aa} = -46.82 \pm 0.05$ cm^{-1}, is observed; this value is more naturally interpreted as the upper state spin-orbit splitting, $A_{\mathrm{SO}} = -46.82$ cm^{-1}.

B. Vibrational structure

The next step in characterizing the excited electronic state is an analysis of the vibrational structure in the PFY spectrum, Fig. 4. A four-atom linear molecule has seven vibrational degrees of freedom: three stretching modes of σ symmetry and two doubly degenerate bending modes of π symmetry. The most important pattern in the spectrum of Fig. 4 is a 1035-cm^{-1} progression (see comb in Fig. 4) which begins with the F_1 and F_2 branches of Fig. 5(a) centered at 33 424 cm^{-1}. If the entire PFY spectrum is displaced 1035 cm^{-1} to the blue, a one-to-one correlation is found with the original spectrum for almost all the peaks, which are combination bands between modes of lower frequency and this main progression. Since ν_2 (the asymmetric CCO stretch) in the ground state has a much higher frequency[11] of 2023 cm^{-1}, the 1035 cm^{-1} progression in the excited state is assigned to ν_3, the symmetric CCO stretch, in reasonable agreement with the harmonic value, 1097 cm^{-1}, calculated by Szalay *et al.*[37] The extensive low-frequency structure in Fig. 4 must therefore result from excitation of the bending modes, an expected result for a linear←bent electronic transition.

In Fig. 4, the lowest member of the ν_3 progression is labeled as the vibrational origin. This assignment requires some justification, since it is possible that these transitions are simply the lowest energy absorptions which lead to dissociation. We showed that the band in Fig. 5(a) is a K'

$=1\leftarrow K''=1$ transition and pointed out that this is consistent with the upper level being the $v=0$ level of a $^2\Pi$ electronic state. Transitions with $K'=1$ could be observed if an even number of bending quanta were excited in the upper state. However, the combination of spin-orbit effects and Renner–Teller coupling[57] in such states should result in additional rotational bands, separated by $\approx 1-3\ \mathrm{cm}^{-1}$ from the F_1 and F_2 branches.[58] The absence of these additional bands in Fig. 5(a) is evidence that no bending quanta are excited in the upper state. It is also possible that only the ν_3 stretching mode is excited in the upper state. However, the two branches centered at 33 424 cm^{-1} are isolated, with no strong transitions nearby. There are, in contrast, several peaks just to the blue of all the higher members of the 3_0^n progression; these are probably bending overtones built on (v_3-1) stretch levels. The absence of such features near the lowest member of this progression supports our assignment of the vibrational origin. Laser induced fluorescence experiments are currently in progress to confirm this assignment.[59]

Given that the ν_3 mode is responsible for the 1035 cm^{-1} progression, it follows that all the transitions below 34 400 cm^{-1} should arise from π bending modes. Note that in a linear←bent transition, odd as well as even quanta may be excited in the bending modes ν_4 and ν_5. However, these transitions do not follow a simple harmonic pattern because the vibrational term values are perturbed by the Renner–Teller interaction.[60] Building a progression in ν_3, ν_4, and ν_5, in which both the spin-orbit and Renner–Teller interactions are incorporated,[61] we can assign most of the larger features from the origin to 36 500 cm^{-1}, Fig. 4. The spectroscopic parameters used are: $\omega_3=1035\ \mathrm{cm}^{-1}$, $\omega_4=416\ \mathrm{cm}^{-1}$, $\epsilon_{\mathrm{RT}}=-0.36$, and $\omega_5=365\ \mathrm{cm}^{-1}$, $\epsilon_{\mathrm{RT}}=0$. The corresponding *ab initio* values[37] are: $\omega_3=1097\ \mathrm{cm}^{-1}$, $\omega_4=328\ \mathrm{cm}^{-1}$, $\epsilon_{\mathrm{RT}}=-0.573$ and $\omega_5=525\ \mathrm{cm}^{-1}$, $\epsilon_{\mathrm{RT}}=-0.017$. Although some transitions are not predicted (most notably the peaks in the range of 34 200–34 300 cm^{-1} and 35 180–35 320 cm^{-1}), there is reasonable agreement between the data and our vibrational assignment. However, many of the assigned peaks lie very near one another, so our labeling scheme must be considered somewhat tentative.

C. Translational energy distributions

In this section, the assignment of the various features in the $P(E_T)$ distributions is considered. In our previous communication, we pointed out that using the heat of formation of HCCO determined in Ref. 26, the maximum translational energies associated with the low and high energy features in the $P(E_T)$ distributions in Figs. 6(a)–(c) correspond to the maximum allowed values for channels II and I, respectively. On this basis, the feature at higher translational energy was assigned to the CH($X\ ^2\Pi$)+CO channel, and the lower energy feature to the CH($a\ ^4\Sigma^-$)+CO channel. Having made this assignment, we can determine the C–C bond strength directly from the $P(E_T)$ distributions, with the goal of obtaining an improved value of the bond strength and heat of formation of the radical.

The values of $E_T^{\max}$, the maximum observed E_T, are measured for both channels in Figs. 6(a)–(c), and for channel I only at higher photon energies. The values of ΔH_0 for the C–C bond cleavage are obtained by conservation of energy,

$$\Delta H_0 = h\nu - E_T^{\max}. \tag{5}$$

Consistency in ΔH_0 is shown at all photon energies, with the mean values of $\Delta H_0(\mathrm{I})=3.1\pm0.2$ eV and $\Delta H_0(\mathrm{II})=3.86\pm0.03$ eV. In practice the value of ΔH_0 for channel II is determined with greater precision than that for channel I because of the sharp cutoff at $E_T^{\max}$ for channel II seen in Figs. 6(a)–(c). One then obtains the heat of reaction for channel I from $\Delta H_0(\mathrm{I})=\Delta H_0(\mathrm{II})-T_0[\mathrm{CH}a(^4\Sigma^-)]$, where the last term is the doublet–quartet splitting in the CH radical of 0.742 ± 0.008 eV.[62,63] Finally, we deconvolute the experimental resolution from the thermodynamic limit to obtain the final values given in the introduction for $\Delta H_0(\mathrm{I})$ and $\Delta H_0(\mathrm{II})$. The thresholds $(hv-\Delta H_0)$ for both channels are indicated by the vertical dashed lines at each photon energy in Fig. 6.

Together with $\Delta H^\circ_{f,0}(\mathrm{CH})=6.149\pm0.013$ eV[64,65] and $\Delta H^\circ_{f,0}(\mathrm{CO})=-1.180\pm0.002$ eV[65] we obtain $\Delta H^\circ_{f,0}$ (HCCO)$=1.83\pm0.03$ eV. This value differs slightly from the heat of formation reported in our previous paper[8] (1.82 ±0.03) due to the use of a more accurate value for $\Delta H^\circ_{f,0}(\mathrm{CH})$ in the thermochemical cycle. From calculated vibrational frequencies of HCCO we obtain the $H^\circ_{298}-H^\circ_0$ value for ketenyl, which, together with tabulated values for CH and CO,[65] gives $\Delta H^\circ_{f,298}(\mathrm{HCCO})=1.83\pm0.03$ eV. Note that the numerical value is the same as at 0 K purely by coincidence. Our heat of formation is similar to the previous determination by photoelectron spectroscopy of $\Delta H^\circ_{f,298}(\mathrm{HCCO})=1.84\pm0.09$ eV,[26] but disagrees with the value of $\Delta H^\circ_{f,298}(\mathrm{HCCO})=1.25\pm0.09$ eV obtained from mass spectrometric appearance potentials.[66] The direct measurement of the C–C bond strength in our experiment gives us confidence that the value reported in this paper represents the most accurate heat of formation for the ketenyl radical to date.

We next consider the broad peak at $E_T=0.9$ eV. At the lowest photon energies where this peak is seen [Figs. 6(d),(e)], it must be due to channel I products, as channel II is not accessible at this translational energy. At still higher excitation energy shown in Figs. 6(f)–(k), one cannot make an unambiguous assignment, but because the peak remains at $E_T=0.9$ eV it is likely that this feature still represents primarily channel I dissociation.

Finally, we consider form of the $P(E_T)$ distributions. The vibrational term values for CH $X(^2\Pi)$(0.35 eV), CH $a(^4\Sigma^-)$(0.39 eV), and CO (0.27 eV) are significantly larger than our experimental translational energy resolution of 0.02 eV (for a $E_T=1$ eV), but no vibrational resolution in observed in the $P(E_T)$ distributions. This observation implies that the CH and/or CO fragments contain substantial amounts of rotational energy.

V. DISCUSSION

A. Spectroscopy of the ketenyl radical

1. Nature of the excited electronic state

In Sec. IV A, the HCCO excited state probed in these experiments was assigned as a $^2\Pi$ state. From the molecular orbital configurations given in Table I, the ultraviolet $\tilde{B}(^2\Pi)$-$\tilde{X}(A'')$ transition in HCCO corresponds to promotion of an electron from $1\pi_{x,y}\rightarrow 2\pi_{x,y}$ orbitals. This effectively promotes an electron from the CO bonding orbital, to a CC bonding/CO antibonding orbital, decreasing r_{CC} and increasing r_{CO} as shown in Fig. 1.

Our spectroscopic results can be compared to two *ab initio* calculations that reached somewhat different conclusions about the geometrical nature of the electronically excited doublet states of HCCO. Using a multi-reference configuration interaction (MR-CI) method, Kim and Shavitt[33] predicted that the excited $^2\Pi$ state is split by Renner–Teller coupling, resulting in a bent $\tilde{B}(^2A')$ state and a linear $\tilde{C}(^2A'')[^2\Pi]$ state. The adiabatic energies for the $\tilde{B}(^2A')\leftarrow\tilde{X}(^2A'')$ and $\tilde{C}(^2A'')[^2\Pi]\leftarrow\tilde{X}(^2A'')$ were predicted to occur at 33 000 cm^{-1} and 33 300 cm^{-1}, respectively. More recently, Szalay *et al.*[37] have performed calculations on the excited states of HCCO using the equation-of-motion ionization-potential coupled cluster singles and doubles (EOMIP-CCSD) method. They demonstrate the bent vs linear equilibrium geometry for the $\tilde{B}$ state is dependent on the choice of basis set. They conclude that the states labeled $\tilde{B}$ and $\tilde{C}$ by Kim and Shavitt are not electronically separate states, but share an identical linear equilibrium geometry and therefore propose the label $2(^2\Pi)$ for this electronic configuration. In our vibrational analysis, a Renner parameter less than unity ($\epsilon_{\mathrm{RT}}=0.36$) was derived, denoting that both components of the $^2\Pi$ state are linear, in agreement with Szalay *et al.*[37] Their calculated spin-orbit splitting for this state, -78 cm^{-1}, is somewhat larger than our value (-46.76 cm^{-1}) but in the right range.

Based on the assignments of Kim and Shavitt,[33] we previously[8] assigned the band in Fig. 3 to the $\tilde{C}(^2A'')[^2\Pi]\leftarrow\tilde{X}(^2A'')$ transition. In light of the new results of Szalay *et al.*[37] and our vibrational analysis, we have revised the spectroscopic label of the excited state seen here. We propose the designation $\tilde{B}(^2\Pi)$ which describes the potential in Fig. 1 as the second distinct electronically excited state of HCCO. Thus the spectrum in Fig. 3 is denoted as the $\tilde{B}(^2\Pi)\leftarrow\tilde{X}(^2A'')$ transition.

2. Comparison with previous experimental investigations

None of the results presented here on the ultraviolet spectroscopy of the HCCO radical are consistent with the absorption spectrum attributed to HCCO by Krishnamachari and Venkatasubramanian.[12] They assigned two band origins at 27 262 cm^{-1} and 29 989 cm^{-1}. Based on gross rotational structure, they proposed for the lower energy band that at least one of the two combining states has a linear geometry, while the second band is assigned to a combination of two nonlinear states. The energetics of these absorption bands are clearly not in agreement with our data. Moreover, the spectrum seen in our photofragment yield measurement was not observed in the absorption experiment, even though the appropriate spectral region was examined. Therefore, we can offer no explanation for the bands observed by Krishnamachari and Venkatasubramanian. It is likely that the carrier of these bands is not the HCCO radical; if this radical were present in their experiment, then the band in Fig. 3 would have been observed. We emphasize again that our experiments are performed on a *mass-selected* beam of radicals, ensuring that the species we probe is indeed HCCO.

B. Photodissociation dynamics

The $P(E_T)$ distributions imply that at least two dissociation mechanisms exist for HCCO radicals excited to the $\tilde{B}(^2\Pi)$ state, leading to channels I and II. The spin-forbidden process, channel II, can result from intersystem crossing (ISC) to the HCCO $\tilde{a}(^4A'')$ surface, followed by dissociation to CH $a(^4\Sigma^-)+\mathrm{CO}$. Calculations by Hu *et al.*[35] predict that the quartet surface correlates to channel II products with either no exit barrier or at most a small barrier no larger than 0.1 eV, although a recent calculation by Yarkony finds a 0.16 eV barrier.[39] The spin-allowed process, channel I, is most likely due to internal conversion (IC) to the ground electronic state followed by dissociation to CH $X(^2\Pi)+\mathrm{CO}$. An alternate mechanism would be one in which the $\tilde{B}(^2\Pi)$ state intersects a repulsive state that correlates to channel I products, although calculations do not support the existence of repulsive states correlating to CH $X(^2\Pi)+\mathrm{CO}$ (see Fig. 1).

The translational energy distributions show that ISC dominates at the three lowest photon energies, but that IC to channel I dominates at higher photon energies. Dissociation proceeding via IC appears to have two components: one leading to the peak at $E_T=0.9$ eV, which does not shift in translational energy for a wide range of excitation energies, and the other resulting in a broad feature underneath this peak which appears to extend across the entire $P(E_T)$ distribution, up to the value of $E_T^{\max}$ for channel I. An overall mechanism should be able to explain the competition between IC and ISC dissociation as well as the two components of the IC process.

The competition between ISC and IC has been considered at length in the context of radiationless transitions from the first excited singlet state (the S_1 state) in aromatic molecules.[67] Each rate is determined primarily by the product of an electronic matrix element between the initial and final electronic state and a series of Franck–Condon factors between the initial and final vibrational levels. The electronic matrix element for IC is generally substantially larger than for ISC because the spin multiplicity is unchanged. However, in aromatic molecules, the geometries of S_1 and T_1 states are quite similar, resulting in considerably higher Franck–Condon factors for ISC than for IC. For naphthalene, the resulting competition between these two compensating effects is that ISC and IC are equally important near the origin of the $S_1 \leftarrow S_0$ transition, but IC becomes progressively more important with increasing vibrational excitation in the S_1 statess as the Franck–Condon factors for IC increase more rapidly than for ISC.[68]

In HCCO, the energetic ordering of electronic states is analogous to that in aromatic molecules, with $\tilde{B}(^2\Pi) > \tilde{a}(^4A'') > \tilde{X}(^2A'')$. However, the Franck–Condon overlap between the vibrational levels of the three states is more difficult to assess due to large geometry differences between these states. The competition between ISC and IC appears to be similar to that in aromatics but more extreme; in HCCO there is very little IC near the $\tilde{B} \leftarrow \tilde{X}$ origin, and IC rapidly becomes dominant with increasing excitation in the $\tilde{B}(^2\Pi)$ state. This implies a very large increase in Franck–Condon factors between the $\tilde{B}(^2\Pi)$ and $\tilde{X}(^2A'')$ states as the excitation energy increases. While it is likely that the same general principles govern the relative rates of ISC and IC in HCCO as in larger aromatic molecules, the nearly complete suppression of IC near the band origin is an unusual feature of the HCCO dissociation dynamics that deserves future consideration.

We next consider the dynamics of IC to yield channel I products. Based on the potential energy surfaces in Fig. 1, one might expect internal conversion to the ground state to be followed by statistical dissociation to products. Our *ab initio* calculations and the CH$(v=1)+$CO vibrational relaxation results of Herbert *et al.*[25] indicate no barrier to dissociation on the ground state surface, so that the translational energy distribution may be predicted using phase space theory[69] or, at a simpler level, a prior distribution.[70] In fact, the broad feature in the higher photon energy $P(E_T)$ distributions [Figs. 6(f)–(k)] can be satisfactorily reproduced by a prior distribution, as shown explicitly in Fig. 6(j), where the prior distribution

$$P^0(E_T) \propto \sum_{v_{\mathrm{CO}}, v_{\mathrm{CH}}=0}^{v_{\max};\ E_v < E_{\mathrm{avail}} - E_T} \sqrt{E_T(v_{\mathrm{CO}}, v_{\mathrm{CH}})} \tag{6}$$

is shown superimposed on the experimental $P(E_T)$ distribution. The prior distribution takes this simple form because both fragments are diatomic molecules, whose classical rotational density of states, $\rho(E_{\mathrm{ROT}})$, is independent of energy.

The second feature associated with IC, the peak at $E_T = 0.9$ eV, is more problematic. This peak does not shift substantially with excitation energy. This trend would be expected for statistical dissociation over a barrier of at least 0.9 eV with respect to products,[14,71] but no barrier to dissociation is present on the potential energy surfaces of either $\tilde{X}\ ^2A''$ or $\tilde{A}\ ^2\Pi$ states (Sec. III C). One must therefore attribute the peak at $E_T = 0.9$ eV to a nonstatistical dissociation process. It appears that internal conversion results in two ensembles, one of which undergoes statistical decay, yielding the broad feature described in the preceding paragraph, while the other undergoes nonstatistical decay and results in a fixed amount of translational energy release over a wide range of excitation energies. The detailed mechanism of the latter process is not clear as of yet and awaits further characterization of the potential energy surfaces involved in HCCO photodissociation.

Finally, we compare the photodissociation dynamics of HCCO with two radicals of similar size, the vinoxy radical, CH_2CHO, and the methoxy radical, CH_3O. All three radicals undergo predissociation at excitation energies around 4 eV, but the dissociation dynamics subsequent to electronic excitation are quite different. The $P(E_T)$ distributions for $CH_3O \rightarrow CH_3 + O$ show that the $\tilde{A}\ ^2A_1$ excited state of CH_3O is predissociated to these products by one or more repulsive states, and that no internal conversion to the ground state occurs.[15] In contrast, the CH_2CHO radical appears to dissociate entirely by internal conversion to the ground state, followed by statistical dissociation to CH_3+CO and $H+CH_2CO$ products.[14] The HCCO radical falls between these extremes, with some dissociation occurring on the $\tilde{a}(^4A'')$ excited state, yielding CH $(a\ ^4\Sigma^-)$ $+$CO products, some occurring statistically on the ground state, yielding a feature in the $P(E_T)$ distribution that can be fit by a prior distribution, and a nonstatistical process on the ground state surface. These three examples illustrate the diverse and complex photodissociation dynamics of open shell species that arise from the relatively large number of low-lying potential energy surfaces compared to closed-shell molecules of comparable size.

VI. CONCLUSIONS

We have investigated the spectroscopy and photodissociation dynamics of the $\tilde{B}(^2\Pi) \leftarrow \tilde{X}(^2A'')$ transition of HCCO, utilizing the method of fast beam photofragment translational spectroscopy on a mass-selected, internally cold sample of ketenyl radicals. Rotational analysis of the photofragment yield spectrum shows that the excited state is linear, with $^2\Pi$ symmetry. Linewidth measurements give a lower bound on the lifetime of the 0_0^0 transition of $\tau \geqslant 300$ ps, suggesting the possibility of studying this transition with laser induced fluorescence. A limited vibrational analysis allows us to assign the symmetric CCO stretch, $\omega_3 = 1035\ \mathrm{cm}^{-1}$. It is also clear from the complications in the PFY spectrum that at least one of the bending modes in the excited state is affected by the Renner–Teller interaction.

The photodissociation dynamics of the HCCO radical are probed by measuring the translational energy and angular distributions of the CH+CO fragments. The spin-forbidden product channel, CH $a(^4\Sigma)+$CO, dominates for excitation energies within the first $1000\ \mathrm{cm}^{-1}$ above the origin, while the spin-allowed channel, CH $X(^2\Pi)+$CO, is the major channel at all higher excitation energies. We propose that the spin-forbidden channel occurs via intersystem crossing to the low-lying $\tilde{a}(^4A'')$ state, and that the spin-allowed channel results from internal conversion to the $\tilde{X}(^2A'')$ state, which correlates without a barrier to CH $X(^2\Pi)+$CO. Although ISC dominates at excess energies below $1000\ \mathrm{cm}^{-1}$, the rapid rise in the internal conversion rate at higher excess energies indicates that the Franck–Condon overlap between the $\tilde{B}$ and $\tilde{X}$ states increases much faster with photon energy than the overlap between the $\tilde{B}$ and $\tilde{a}$ states. The translational energy distributions for the CH $X(^2\Pi)+\mathrm{CO}$ products indicate that both statistical and nonstatistical dissociation occurs following internal conversion. A more complete understanding of the photodissociation dynamics will require further experimental and theoretical investigations of HCCO, and the authors hope that the work presented here will stimulate such studies.

ACKNOWLEDGMENTS

This research is supported by the Director, Office of Energy Research, Office of Basic Energy Sciences, Chemical Sciences Division, of the U.S. Department of Energy under Contract No. DE-AC03-76SF00098. We acknowledge helpful conversations with Professors Robert Curl, Richard Dixon, Yasuki Endo, and Donald Levy. We thank Professors Isaiah Shavitt and Peter Szalay for sharing their results prior to publication.

[1] J. Warnatz, *Combustion Chemistry*, edited by W. C. Gardiner (Springer, Berlin, 1984), p. 288.

[2] J. V. Michael and A. F. Wagner, J. Phys. Chem. **94**, 2453 (1990).

[3] W. Boullart and J. Peeters, J. Phys. Chem. **96**, 9810 (1992).

[4] J. Peeters, I. Langhans, and W. Boullart, Int. J. Chem. Kinet. **26**, 869 (1994).

[5] C. K. Westbrook and F. L. Dryer, *Eighteenth Symposium (International) on Combustion* (Combustion Institute, Pittsburgh, 1981), p. 749.

[6] K. Brezinsky, Prog. Energy Combust. Sci. **12**, 1 (1986).

[7] J. A. Miller, R. J. Kee, and C. K. Brook, Ann. Rev. Phys. Chem. **41**, 245 (1990).

[8] D. H. Mordaunt, D. L. Osborn, H. Choi, R. T. Bise, and D. M. Neumark, J. Chem. Phys. **105**, 6078 (1996).

[9] Y. Endo and E. Hirota, J. Chem. Phys. **86**, 4319 (1987); Y. Ohshima and Y. Endo, J. Mol. Spec. **159**, 458 (1993).

[10] H. E. Radford, 21st International Symposium on Free Radicals, Williamsburg, MA (1991).

[11] K. G. Unfried, G. P. Glass, and R. F. Curl, Chem. Phys. Lett. **177**, 33 (1991); K. G. Unfried and R. F. Curl, J. Mol. Spec. **150**, 86 (1991).

[12] S. L. N. G. Krishnamachari and R. Venkatasubramanian, Pramana **23**, 321 (1984).

[13] G. Inoue and M. Suzuki, J. Chem. Phys. **84**, 3709 (1986).

[14] D. L. Osborn, H. Choi, D. H. Mordaunt, R. T. Bise, D. M. Neumark, and C. M. Rohlfing, J. Chem. Phys. **106**, 3049 (1997); D. L. Osborn, H. Choi, and D. M. Neumark, Adv. Chem. Phys. (in press).

[15] D. L. Osborn, D. J. Leahy, E. M. Ross, and D. M. Neumark, Chem. Phys. Lett. **235**, 484 (1995); D. L. Osborn, D. J. Leahy, and D. M. Neumark, J. Phys. Chem. (in press).

[16] I. T. N. Jones and K. D. Bayes, J. Am. Chem. Soc. **94**, 6869 (1972).

[17] W. Boullart, M. T. Nguyen, and J. Peeters, J. Phys. Chem. **98**, 8036 (1994).

[18] J. Peeters, I. Langhans, W. Boullart, M. T. Nguyen, and Katia Devriendt, J. Phys. Chem. **98**, 11 988 (1994).

[19] J. Peeters, W. Boullart, and Katia Devriendt, J. Phys. Chem. **99**, 3583 (1995).

[20] D. G. Williamson and K. D. Bayes, J. Phys. Chem. **73**, 1232 (1969).

[21] A. M. Schmoltner, P. M. Chu, and Y. T. Lee, J. Chem. Phys. **91**, 5365 (1989).

[22] F. Temps, H. Gg. Wagner, and M. Wolf, Z. Phys. Chem. **176**, 27 (1992).

[23] K. K. Murray, K. G. Unfried, G. P. Glass, and R. F. Curl, Chem. Phys. Lett. **192**, 512 (1992).

[24] C. Vinckier, M. Schaekers, and J. Peeters, J. Phys. Chem. **89**, 508 (1985).

[25] L. B. Herbert, I. R. Sims, I. W. M. Smith, D. W. A. Stewart, A. C. Symonds, A. Canosa, and B. R. Rowe, J. Phys. Chem. **100**, 14 928 (1996).

[26] J. M. Oakes, M. E. Jones, V. M. Bierbaum, and G. B. Ellison, J. Phys. Chem. **87**, 4810 (1983).

[27] M. A. Hanratty and H. H. Nelson, J. Chem. Phys. **92**, 814 (1990); G. Inoue and M. Suzuki, J. Chem. Phys. **92**, 815 (1990).

[28] M. E. Jacox and W. B. Olson, J. Chem. Phys. **86**, 3134 (1987).

[29] L. B. Harding, J. Phys. Chem. **85**, 10 (1981).

[30] D. L. Cooper, Astrophys. J. **265**, 808 (1983).

[31] L. B. Harding and A. F. Wagner, J. Phys. Chem. **90**, 2974 (1986).

[32] J. D. Goddard, Chem. Phys. Lett. **154**, 387 (1989).

[33] K. Kim and I. Shavitt, private communication.

[34] P. G. Szalay, J. F. Stanton, and R. J. Bartlett, Chem. Phys. Lett. **193**, 573 (1992).

[35] C. H. Hu, H. F. Schaefer, Z. Hou, and K. D. Bayes, J. Am. Chem. Soc. **115**, 6904 (1993).

[36] M. T. Nguyen, W. Boullart, and J. Peeters, J. Phys. Chem. **98**, 8030 (1994).

[37] P. G. Szalay, G. Fogarasi, and L. Nemes, Chem. Phys. Lett. **263**, 91 (1996).

[38] P. G. Szalay and J. P. Blaudeau, J. Chem. Phys. **106**, 436 (1997).

[39] D. Yarkony, J. Phys. Chem. **100**, 17 439 (1996).

[40] C. P. Fenimore and G. W. Jones, J. Chem. Phys. **39**, 1514 (1963).

[41] V. Zengin, B. J. Persson, K. M. Strong, and R. E. Continetti, J. Chem. Phys. **105**, 9740 (1996).

[42] H. Choi, D. H. Mordaunt, R. T. Bise, and D. M. Neumark (in preparation).

[43] R. E. Continetti, D. R. Cyr, D. L. Osborn, D. J. Leahy, and D. M. Neumark, J. Chem. Phys. **99**, 2616 (1993).

[44] R. E. Continetti, D. R. Cyr, R. B. Metz, and D. M. Neumark, Chem. Phys. Lett. **182**, 406 (1991).

[45] D. L. Osborn, D. J. Leahy, D. R. Cyr, and D. M. Neumark, J. Chem. Phys. **104**, 5026 (1996).

[46] J. M. B. Bakker, J. Phys. E. **6**, 785 (1973); *ibid.*, **7**, 364 (1974).

[47] D. J. Leahy, D. L. Osborn, D. R. Cyr, and D. M. Neumark, J. Chem. Phys. **103**, 2495 (1995).

[48] D. P. de Bruijn and J. Los, Rev. Sci. Instrum. **53**, 1020 (1982).

[49] S. Gerstenkorn and P. Luc, *Atlas du Spectre d'Absorption de la Molecule d'Iode* (Centre National de la Recherche Scientifique, Paris, 1978).

[50] R. N. Zare, Mol. Photochem. **4**, 1 (1972).

[51] D. Hegarty and M. A. Robb, Mol. Phys. **38**, 1795 (1979); R. H. E. Eade and M. A. Robb, Chem. Phys. Lett. **83**, 362 (1981).

[52] GAUSSIAN 94, Revision C.3, M. J. Frisch, G. W. Trucks, H. B. Schlegel, P. M. W. Gill, B. G. Johnson, M. A. Robb, J. R. Cheeseman, T. Keith, G. A. Petersson, J. A. Montgomery, K. Raghavachari, M. A. Al-Laham, V. G. Zakrzewski, J. V. Ortiz, J. B. Foresman, J. Cioslowski, B. B. Stefanov, A. Nanayakkara, M. Challacombe, C. Y. Peng, P. Y. Ayala, W. Chen, M. W. Wong, J. L. Andres, E. S. Replogle, R. Gomperts, R. L. Martin, D. J. Fox, J. S. Binkley, D. J. Defrees, J. Baker, J. P. Stewart, M. Head-Gordon, C. Gonzalez, and J. A. Pople, Gaussian, Inc., Pittsburgh PA, 1995.

[53] G. Herzberg, *Molecular Spectra and Molecular Structure III. Electronic Spectra and Electronic Structure of Polyatomic Molecules* (Van Nostrand, Princeton, 1966).

[54] J. K. G. Watson, *Vibrational Spectra and Structure*, edited by J. R. Durig (Elsevier, Amsterdam, 1977), Vol. 6, pp. 2–89.

[55] W. T. Raynes, J. Chem. Phys. **41**, 3020 (1964).

[56] E. Hirota, *High Resolution Spectroscopy of Transient Molecules* (Springer, Heidelberg, 1985).

[57] Ref. 53, p. 35.

[58] The splitting is given approximately by $3/16\sqrt{2}\,A_{\mathrm{SO}}\epsilon_{\mathrm{RT}}$, where A_{SO} is the spin-orbit splitting and ϵ_{RT} is the Renner parameter. See G. Herzberg, *Molecular Spectra and Molecular Structure III. Electronic Spectra and Electronic Structure of Polyatomic Molecules* (Van Nostrand, Princeton, 1966), pp. 34–37.

[59] L. R. Brock, B. Mischler, E. A. Rohlfing, R. T. Bise, and D. M. Neumark, J. Chem. Phys. (submitted).

[60] R. Renner, Z. Phys. **92**, 172 (1934).

[61] J. A. Pople, Mol. Phys. **3**, 16 (1960); J. T. Hougen, J. Chem. Phys. **36**, 519 (1962).

[62] S. G. Lias *et al.*, J. Chem. Phys. Ref. Data **17**, Suppl. No. 1 (1988).

[63] A. Kasdan, E. Herbst, and W. C. Lineberger, Chem. Phys. Lett. **31**, 78 (1975).

[64] M. Danielsson, P. Erman, A. Hishikawa, M. Larsson, E. Rachlew-Källne, and G. Sundström, J. Chem. Phys. **98**, 9405 (1993).

[65] M. W. Chase, Jr., C. A. Davies, J. R. Downey, Jr., D. J. Frurip, R. A. McDonald, and A. N. Syverud, JANAF Thermochemical Tables, 3rd ed., J. Chem. Phys. Ref. Data **14**, (1985), Suppl. No. 1.

[66] J. L. Holmes and F. P. Lossing, Int. J. Mass. Spectrom. Ion Process. **58**, 113 (1984).

[67] P. Avouris, W. M. Gelbart, and M. A. El-Sayed, Chem. Rev. **77**, 793 (1977); *ibid., Radiationless Transitions*, edited by S. H. Lin (Academic, New York, 1980).

[68] G. S. Beddard, G. R. Fleming, O. L. J. Gijzeman, and G. Porter, Chem. Phys. Lett. **18**, 481 (1973).

[69] J. C. Light, Discuss. Faraday Soc. **44**, 14 (1977).

[70] R. D. Levine and J. L. Kinsey, in *Atom-Molecule Collision Theory—A Guide for the Experimentalist*, edited by R. B. Bernstein (Plenum, New York, 1979).

[71] A. M. Wodtke, E. J. Hintsa, and Y. T. Lee, J. Phys. Chem. **90**, 3549 (1986); X. Zhao, R. E. Continetti, A. Yokoyama, E. J. Hintsa, and Y. T. Lee, J. Chem. Phys. **91**, 4118 (1989).